4. Beamlines

This section describes the activity status of the light source and optics of the beamlines in FY2020. It includes the insertion device (ID), frontend, optics and transport channel, radiation shielding of SPring-8, and SACLA beamlines. In addition to routine maintenance, several component upgrades and R&D were performed. Beamline upgrade and portfolio rearrangement are ongoing toward the SPring-8 major upgrade. Some beamline reconstructions were carried out during this period.

1. Insertion device and frontend

1-1. Insertion device

(1) Restoration of the twin helical undulator for BL25SU

The hardware trouble of the insertion device in BL25SU found in the regular maintenance in March 2020 has been fixed. It consists of a pair of helical undulators installed in the same straight section and one of the linear guides in the gap-driving system for the upstream undulator was broken owing to radiation damage. There are more than 10 linear guides of the same type besides the relevant one, and all of them have been replaced with new ones to avoid further potential problems. Because of the complicated mechanical structure, the repair work should be conducted in the factory of the manufacturer, and thus the undulator should be taken out of the accelerator tunnel and transported to the factory. It takes about a few months to complete the whole process, and thus we decided to repair the two undulators alternately to avoid the shutdown of the beamline. Although fast helicity switching is not available, the beamline can be operated with one of the two undulators.

In the summer shutdown, the upstream undulator was taken out and transported to the factory, where the repair work was carried out until the end of November 2020. It was then reinstalled in the storage ring in the winter shutdown. In the same period, the downstream undulator was taken out and its repair work was completed in February 2021. It was reinstalled in March 2021, with which the twin helical undulator for BL25SU was fully restored.

(2) New magnetic circuit for in-vacuum undulators

An in-vacuum undulator (IVU) is nowadays a standard insertion device for high-energy synchrotron radiation, and more than 50 IVUs have been installed in SPring-8 and SACLA. Although the in-vacuum structure significantly reduces the minimum gap, it imposes a stringent requirement on the permanent magnet (PM) material; the coercivity should be sufficiently high to prevent demagnetization during operation. Besides radiation demagnetization, we have to take care of thermal demagnetization, which can potentially occur during the bake-out process for the ultrahigh vacuum conditions required for installation in storage rings. It should be emphasized that the PM blocks used in undulators are exposed to a strong reverse field, which works to accelerate the demagnetization process, and thus they can be demagnetized much more easily than those used alone.

Because the coercivity (H_{cj}) is negatively correlated with the remanent field (B_r), we have to make a compromise in the choice of the PM material. As a result, the B_r of a PM material available for IVUs is relatively lower than that available for out-vacuum undulators, which potentially suppress the achievable performance of IVUs.

To overcome the above difficulty, we have recently proposed a new undulator configuration in which the easy axis of magnetization is tilted by 45 degrees with respect to the original one. Although it has no impact on the peak field strength, it effectively reduces the reverse field applied to each PM block and retards the progress of demagnetization. To demonstrate its performance, we measured the demagnetization rate of undulator samples with the new configuration under high-temperature conditions and compared it with those with the conventional hybrid and Halbach configurations. The experimental results are shown in Fig. 1, where the demagnetization rates are plotted as a function of temperature for the three different samples, showing that the resistance of the new configuration is much higher than those of the other two. It is expected that a PM material with a higher B_r will be available for IVUs if we employ this configuration, leading to a higher undulator performance.

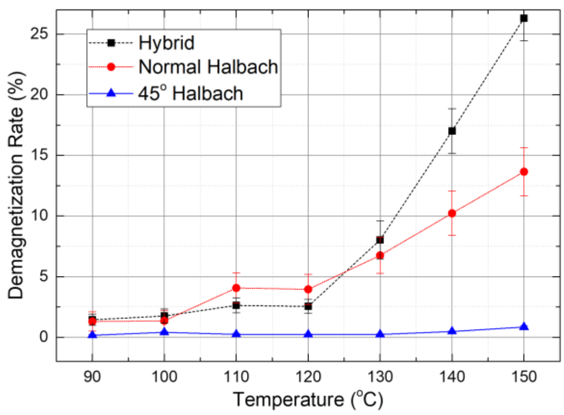

Fig. 1. Experimental demonstration of new undulator configuration to improve resistance against thermal demagnetization.

1-2. Frontend

(1) High-heat-load handling techniques

Fatigue crack growth tests were conducted on GlidCop made by a new manufacturing process in order that the material constants "*C*" and "*m*" for Paris' law, giving the fatigue crack growth length due to a single stress fluctuation, were obtained at room temperature, 200°C, and 400°C. We used these data to perform fatigue life analysis based on the fracture-mechanical technique and then attempted to compare them with the results of cyclic irradiation tests conducted the previous year. It was found that the crack growth life was considerably affected by the shape characteristics (depth and width) of the inclusions when they were treated as initial defects.

(2) X-ray beam position monitor (XBPM)

We have completed our efforts to reduce the impact of changing the filling pattern on the XBPM output value, which have been underway since FY2018. We measured the correction coefficients for all XBPMs at the ID-BLs where the ID gap has been widened to reduce the filling-pattern dependence since last year. In addition, the continuity with past records was suppressed to less than 10 μm for all BLs by "offset adjustment". At the newly constructed BL05XU, we introduced an inclined configuration-type XBPM, which can reduce the influence of filling-pattern changes by mitigating the space charge effect on the detection elements, and confirmed that it operates properly. The detection elements of the pulse-mode XBPM under development were modified to a high-heat-resistance and high-output type. In evaluation tests at BL02B1, it was confirmed that the resolution for each pulse was approximately 10 μm RMS.

(3) New beam profile monitoring system for X-ray beam exiting from the frontend

Aiming at the direct measurement of the photon beam axis exiting from the frontend, we developed a system for visualizing scattered X-rays from a chemical-vapor-deposition diamond thin film through a 50-μm-diameter pinhole at BL05XU. We introduced a direct-detection-type detector, SOPHIAS (Silicon-On-Insulator Photon Imaging Array Sensor) [1, 2], so that the fast energy-resolved beam monitoring could be achieved. It is necessary to deal with the problem of diffraction generated by the crystal grains of the diamond thin film affecting the calculation of the center of the photon beam axis.

2. Optics and transport channel

(1) Analysis of double-crystal monochromator (DCM) vibration

X-ray beams should have high stability, especially for experiments using intense focused beams, which are made by projecting the light source directly. Since a DCM is placed between the light source and focal points, its vibration blurs focuses to increase the effective focus sizes. DCMs have been improved by suppressing coolant turbulence, enhancing stage rigidity, and improving the cooling efficiency. Vibrations were suppressed into approximately 100 nrad (RMS) or less in terms of a relative angular deviation between two crystals. Our targets toward vibration reduction are to 50 nrad in the near future and to 10 nrad finally.

In SPring-8, vibrations of DCMs have been evaluated by monitoring the intensity fluctuations of monochromatic beams. That is because the method is the simplest and applicable in every beamline. If the DCM were the sole vibration source, the intensity fluctuations at the half maximum of a rocking curve profile would be translated into angular vibrations. However, it turns out that the measured intensity fluctuations contain elements that cannot be explained from the DCM vibrations. Some of them result from the instability in the light source. For the effective improvement in the DCMs, the net DCM vibrations should therefore be extracted from the measured fluctuations.

Let $R(\theta)$ be an intensity profile of the rotation angle θ of the first crystal. When the relative angle between the two crystals rocks by $\delta\theta$, the intensity fluctuates by $R(\theta+\delta\theta) - R(\theta) = R'\delta\theta$, where the derivative is operated with respect to θ. The intensity fluctuation caused by the DCM is proportional to R'. As a result, its power spectrum is expressed as R'^2 times that of the angular fluctuation. Instability except for the DCM does not show R'^2 dependence. The spectrum of the angular fluctuation of the DCM can be distinguished accordingly.

The test experiment was carried out for 1.5 Å X-rays at BL13XU. The beam intensity was measured with a silicon PIN photodiode at a sampling rate of 1 kHz. The first crystal was shifted every 0.2” (~1 mrad) at a time interval of 5.5 s. Figure 2(a) shows the measured intensity, (b) the extraction of the intensity fluctuation, and (c) the map arranging the power spectrum at each angular position. The beam intensity decreased frequently because of the top-up injection to the storage ring, and then the spectra were different from the others, as shown by the vertical lines in the spectral map, which came from the light source. In the spectral map, the component at 110 Hz was larger at the half maximums of the rocking curve than at the peak, which was characteristic of the DCM vibration. On the other hand, the components at 20 and 40 Hz did not result from the DCM because they were larger at the peak. The spectrum of the DCM vibration (Fig. 3) was extracted by the numerical method of non-negative matrix factorization. The DCM vibration was calculated to be 87 nrad.

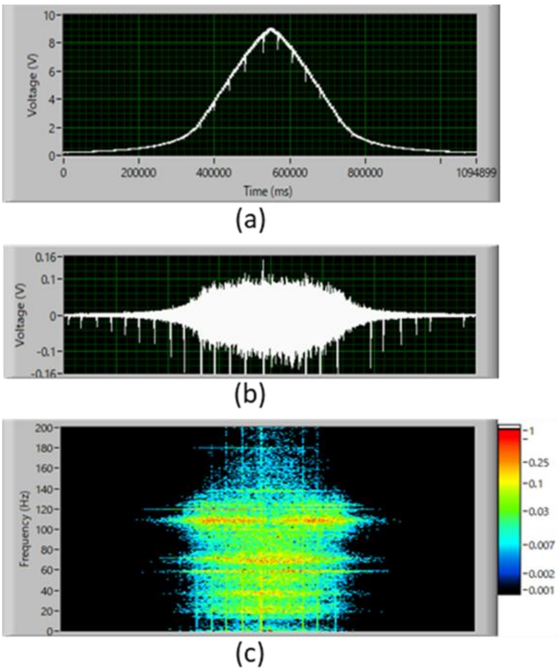

Fig. 2. (a) Measured intensity, (b) intensity fluctuation, and (c) spectral map of the fluctuation.

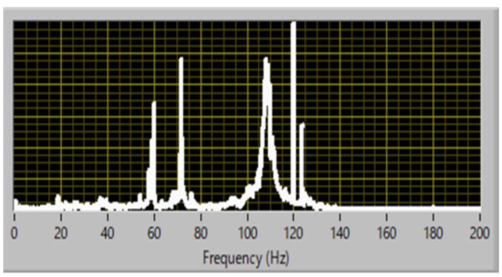

Fig. 3. Calculated spectrum of DCM vibration.

(2) Upgrade of high-energy optics in BL05XU

BL05XU aims at the research and development of X-ray optical elements for the next-generation high-energy high-flux beam and also many types of optical element under high heat load conditions. For this purpose, X-ray optical components in optics hutch 1 (OH1) and optics hutch 2 (OH2) were reconstructed [3].

Commissioning and evaluations of the installed new X-ray optical components (Fig. 4) were started in April 2020. We developed total reflection mirrors and double multilayer monochromators (DMMs) to provide a high-flux beam with an energy bandwidth at ~1%, which is much wider than that provided by a Si DCM. The multilayer mirrors were coated in the SPring-8 optics laboratory. Evaluation results are summarized in Table 1. Figure 5 shows an energy spectrum of an X-ray beam at 100 keV. High-flux beams with a flux from 10^{13} to 10^{15} photons/s were obtained at an X-ray energy from 4.5 to 100 keV.

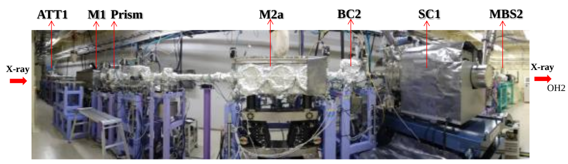

Fig. 4. Photograph of beamline components in OH1. ATT: attenuator; M1, M2a: mirror; SC: silicon-crystal monochromator; BC: beam catcher; MBS2: main beam shutter 2.

Table 1. Evaluated X-ray beams provided by total reflection mirror pair or double multilayer monochromators (DMMs)

Energy (keV)	4.5	19	30	40	100
Mirror/ DMM	Total reflection, Si	Total reflection, Pt	DMM $(W/C)_{20}$	DMM $(W/C)_{20}$	DMM $(Cr/C)_{150}$
Incident angle	4 mrad	4 mrad	4 mrad	3 mrad	1.9 mrad
Flux (photons/s)	1.3×10^{15}	3×10^{13}	1.2×10^{15}	6.5×10^{14}	1.3×10^{13}
Energy bandwidth (%)	1.4	0.9	1.5	1.7	0.93
Undulator	1st harmonic, gap 8.24 mm	3rd harmonic, gap 10.61 mm	3rd harmonic, gap 14.77 mm	3rd harmonic, gap 18.69 mm	19th harmonic, gap 9.41mm

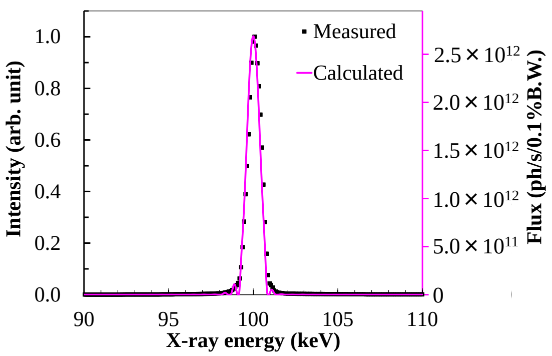

Fig. 5. Energy spectrum of X-ray beam at 100 keV.

Other evaluations of optical elements, including a harmonic separator to extract a specific harmonic from an undulator spectrum and a double-channel cut monochromator to provide an extremely stable beam with a high monochromaticity, are in progress. The mirror deformation caused by a heat load from the undulator was observed in situ with a Fizeau interferometer. The obtained results were used to extend the applicability of computational simulations to estimate heat transfer from the X-ray irradiation area to a cooling medium. Some advanced research studies were started with the high-flux high-energy beam provided by a DMM at an experimental area with dimensions of 3 m × 4 m in OH2. In addition, we installed the other basic and essential optical components with a water cooling system used under high heat load conditions, such as attenuators (diamond, SiC, Si, Mo, and W), beam profile monitors made of diamond, beam intensity monitors made of diamond, beam catchers, a tungsten shutter, and MBS2 (main beam shutter 2). These optical components were evaluated and confirmed to be practical under a high heat load condition up to 300 W.

The alignment mechanism for the first mirror was upgraded in March 2021 from a water-cooling system to a liquid-nitrogen-cooling system to improve stability under higher heat load conditions. Furthermore, we started the design and fabrication of micro-focus optics for a 100-keV beam. These optics will be evaluated in 2021.

(3) Reconstruction of BL09XU

BL09XU was reconstructed to a beamline dedicated for HAXPES application. Figure 6 shows the layout of the upgraded BL09XU. Some components such as double-channel-cut monochromators, X-ray phase retarders, and monitoring systems were newly installed in the optics hutch. A new focusing mirror system was installed in EH1. At the transport channel, ion pumps were adopted as the main vacuum pump. The Be windows between the frontend section and the transport channel were removed to avoid a flux loss at a lower photon energy. A fast-closing valve (FCV), a fast absorber (Fabs), and a differential pumping system (DPS) were installed in place of the Be windows to prevent vacuum trouble. The reconstructions started in February 2021. The commissioning will be started since May 2021. After the short commissioning period, the beamlines will be opened for public use.

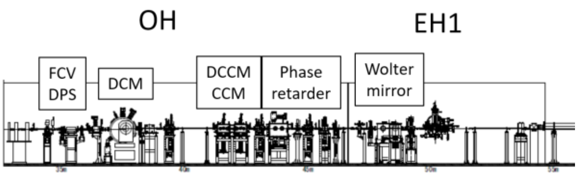

Fig. 6. Layout of upgraded BL09XU (OH and EH1).

(4) Monolithic Wolter mirror as focusing optics for BL09XU

A monolithic Wolter type-I focusing mirror was designed and installed at experimental hutch (EH) 1 of BL09XU. The high repeatability and easy alignment are required for focusing optics in EH1, because the focusing optics is removed when an experiment is carried out at EH2. The tolerance for the alignment error of the Wolter mirror is high owing to its small comatic aberration; hence, the Wolter mirror is adequate for focusing optics in EH1. The fabricated monolithic Wolter mirror consists of ellipsoid and hyperboloid surfaces on a substrate of 550 mm length (Fig. 7). A focused beam size of 26 μm (horizontal) × 1.4 μm (vertical) and a high throughput of 70% are expected.

Fig. 7. Photograph of monolithic Wolter mirror.

(5) Reconstruction of BL35XU

The optics hutch (OH) and experiment hutches (EH1 and EH2) of BL35XU were reconstructed to move applications on nuclear resonant scattering from BL09XU to BL35XU. A focusing mirror and a monitoring system were newly installed in OH, and high-resolution monochromators were moved from EH1 of BL09XU to OH of BL35XU. The DCM was upgraded to manage a high heat load. At the transport channel, ion pumps were adopted as the main vacuum pump. The reconstructions started in December 2020. The commissioning will be started since May 2021. After the short commissioning period, the beamlines will be opened for public use.

(6) Reconstruction of BL20B2

A DMM was designed and installed in the medium-length bending-magnet beamline BL20B2. The DMM increases photon flux density around 40 keV and 110 keV for imaging applications, such as the angiography of small animals, fossils, rocks, and industrial materials with a large field of view. The design parameters of the multilayers are listed in Table 2. The calculated multilayer reflectivity is shown in Fig. 8. The energy resolutions of the designed multilayers are 4.8% and 0.8% for DMM

40 keV and 110 keV, respectively. It is expected that the flux densities will be increased by more than two orders of magnitude compared with that of a Si DCM with narrow energy resolutions of ~0.015% and ~0.001% for Si 111 and 511 reflections, respectively. The DCM still remains available for experiments that require specific energy and a high energy resolution. Figure 9 shows the layout of the newly installed and realigned components at BL20B2 OH. The reconstruction of BL20B2 OH started in December 2020. The commissioning will be started since April 2021. After the short commissioning period, the beamlines will be opened for public use.

Table 2. Parameters of multilayer mirrors

Working photon energy	40 keV	110 keV
Name	M1b, M2b	M1a, M2a
Substrate material	Si	
Substrate size	820 mm long × 80 mm width × 60 mm thick	
Coating	W/B_4C multilayer	
Multilayer period (d)	3.85 nm	1.908 nm
Gamma (W layer thickness / d)	0.5	
Number of periods	50	200
Bragg angle	4.2857 mrad	3 mrad
Energy resolution (ΔE/E)	4.8%	0.8%

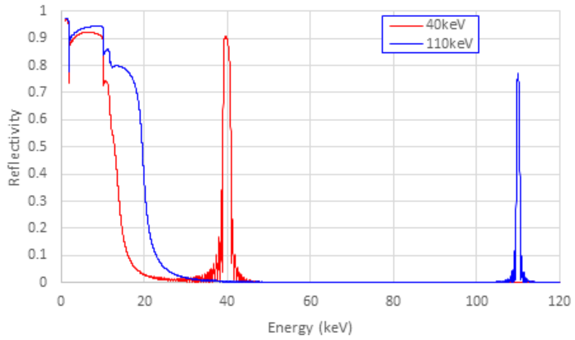

Fig. 8. Calculated reflectivity of multilayers for DMM 40 keV and DMM 110 keV.

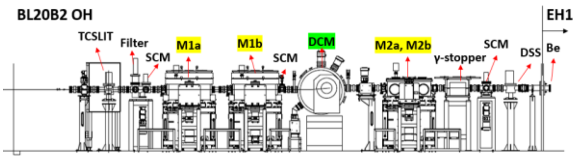

Fig. 9. Layout of newly installed and realigned components at BL20B2 optics hutch.

3. Radiation shielding for SPring-8 beamline

(1) Radiation shielding hutches

To enable the robotic exchange of samples in the experimental hutch during beam on, a sample introduction port was newly developed and installed in the experimental hutch of BL02B1. This port has two pneumatic shutters, each of which has the ability to shield radiation independently. By operating these shutters in sequence, the sample can be replaced without radiation leakage.

(2) Radiation-shielding calculations for applications to the Nuclear Regulation Authority

Radiation-dose calculations for the 48th change permission application were performed. They include the change in the movable end stopper size of BL09XU, lower power revision and the addition of two monochromators of BL20B2, the change from the lead collimator to the tungsten collimator of BL29XU, changes in the positions of the monochromator, gamma stopper, and beamline shutter, and the change in the beamline shutter 2 thickness of BL35XU.

(3) Radiation leakage inspection at beamlines

The following beamlines were inspected: BL01B1, BL13XU, BL22XU (reinstallation of local shield), BL03XU (conversion of cable duct), BL19LXU (adjustment of door position), and BL28XU (conversion of local shield).

(4) Radiation measurements and the development of methods

A beam loss monitor was installed at SSBT. To investigate the radiation tolerance of the LED light and motor driver, GafChromic films were used for dose measurement.

4. Beamlines of SACLA

4-1. XFEL beamlines

In FY2020, the two XFEL beamlines (BL2 and BL3) were stably operated in parallel to produce hard X-ray pulses in the range of 4–20 keV [4]. The main linac of SACLA drives the two beamlines by switching the electron-beam route in a pulse-by-pulse manner. Moreover, the switching operation was expanded to beam injection into the storage ring of SPring-8. The steady operation of both SACLA and SPring-8 has been achieved with the SACLA injection scheme. SACLA will completely take over the role of the conventional SPring-8 injector system (a 1-GeV linac and an 8-GeV booster synchrotron), which had been operated for more than 20 years and will be shut down in 2021. The new injection scheme will contribute to reductions in operating costs. Moreover, the low-emittance beam of the SACLA linear accelerator is required for future upgrades of SPring-8.

For the XFEL transport channels, photon diagnostic systems and optics-tuning software have been upgraded for the automated tuning of the accelerator and beamlines. An auto-tuning method for controlling SACLA operation parameters has been developed using machine learning (ML) techniques, where XFEL characteristics are used as the figure of merit, for example, pulse energies measured with beam monitors and spatial profiles observed with screen monitors. An in-line spectrometer consisting of a nano-diamond foil made by chemical vapor deposition (CVD) and an MPCCD detector is used to monitor the XFEL spectra. The spectrometer can provide information on the peak photon energies with high accuracy; however, it is not suitable for measurements of a detailed spectral shape because the spectral resolution is low (~100 eV) and larger than the typical bandwidths of SASE-XFEL. Therefore, the spectral width remains an uncontrollable characteristic in the auto-tuning method. To obtain single-shot spectra with an improved resolution, a new in-line spectrometer was proposed to use a capillary filled with diamond nanopowders. Here, the spectral resolution is expected to be higher than 10 eV because of the larger grain size of the diamond. In FY2021, a prototype of the spectrometer will be installed at BL3 EH1 for daily tuning after the proof-of-concept demonstration.

4-2. Soft X-ray FEL beamline

The soft X-ray (SX) FEL beamline (BL1) is driven by a dedicated 800-MeV linac (SCSS+) to produce

SX pulses with photon energies of 40–150 eV and pulse widths of ~30 fs [5, 6]. However, the magnet degradation of the undulator caused a considerable decrease in output pulse energy. In FY2020, the undulator line consisting of three undulator units was laterally shifted by 5 mm for the electron beam to avoid the degraded areas of magnets. However, the output pulse energy was not recovered sufficiently. Therefore, in March 2021, the first undulator unit was re-tuned to mitigate the magnet degradation, while the other two units were replaced with the ones from BL2 and BL3 (Fig. 10). In FY2021, the recovery of pulse energy will be confirmed. The effect of the removal of undulator units from BL2 and BL3 is expected to be small because these beamlines still have enough undulator units to reach saturation.

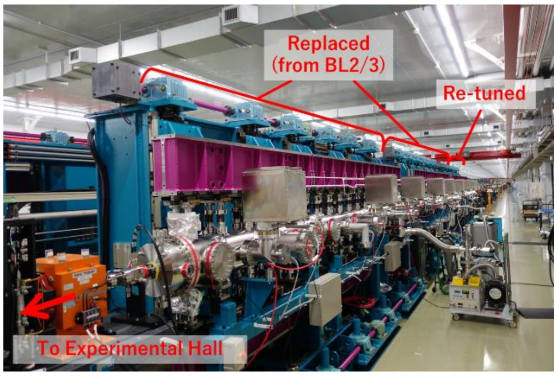

Fig. 10. Replaced undulator units at SACLA BL1.

Takashi Tanaka[*1], Sunao Takahashi[*1], Hirokatsu Yumoto[*1], Takahisa Koyama[*1], Yasunori Senba[*1], Hiroshi Yamazaki[*1], Haruhiko Ohashi[*1], Kunikazu Takeshita[*1], Nobuteru Nariyama[*1], Shunji Goto[*1], Yuichi Inubushi[*2], Shigeki Owada[*2], Toshinori Yabuuchi[*2], Kensuke Tono[*2], and Makina Yabashi[*3]

[*1] Light Source Division, JASRI

[*2] XFEL Utilization Division, JASRI

[*3] XFEL Research and Development Division, RIKEN SPring-8 Center

References:

[1] Hatsui, T. and Graafsma, H. (2015). *IUCrJ*. May 1; 2(Pt 3), 371–383.

[2] Hatsui, T. et al. (2013). *Proceedings of International Image Sensor Workshop*, Online.

[3] Yumoto, H. et al. (2020). *Proc. SPIE* **11492**, 114920I.

[4] Tono, K. et al. (2019). *J. Synchrotron Rad.* **26**, 595–602.

[5] Owada, S. et al. (2018). *J. Synchrotron Rad.* **25**, 282–288.

[6] Owada, S. et al. (2020). *J. Synchrotron Rad.* **27**, 1362–1365.